Resonant MEMS Mass Sensors for Measurement of Microdroplet Evaporation

Kidong Park, Namjung Kim, Dallas T. Morisette, N. R. Aluru, *Fellow, ASME*, and Rashid Bashir, *Fellow, IEEE*

***Abstract*—Microelectromechanical systems (MEMS)-based resonant mass sensors have been extensively studied due to their high sensitivity and small size, making them very suitable for detecting micro- or nanosized particles, as well as monitoring microscaled physical processes. In a range of physical and biological applications, accurate estimation and precise control of the evaporation process of microdroplets are very important. However, due to the lack of appropriate measurement tools, the evaporation process of microdroplets has not been well characterized. Here, we introduce a self-oscillating MEMS mass sensor with a uniform mass sensitivity to directly measure the mass changes of evaporating microdroplets. The mass sensor has a unique spring structure to provide spatially uniform mass sensitivity. The sensor's velocity is fed back to the actuation signal to induce self-oscillation, enabling rapid determination of the resonant frequency. The evaporation rates of single microdroplets of dimethyl sulfoxide and water at various temperatures are obtained. With the measured evaporation rates and the simulated surface area of the microdroplet, the enthalpies of vaporization of both liquids are extracted and found to be in agreement with those in the literature. The method developed in this work can be a valuable tool to enhance our understanding of microscaled physical processes involving rapid mass change, such as evaporation, deposition, self-assembly, cryopreservation, and other biological applications. [2011-0190]**

***Index Terms*—Evaporation, microdroplet, microelectromechanical systems (MEMS), resonant mass sensor.**

Manuscript received June 23, 2011; revised January 12, 2012; accepted February 9, 2012. This work was supported by the National Science Foundation (NSF) under Grants 0810294, 1120597, and EEC-0425626 (NSF Nanoscale Science and Engineering Center at Ohio State University). Subject Editor C. Liu.

K. Park is with the Department of Electrical and Computer Engineering and the Micro and Nanotechnology Laboratory, University of Illinois at Urbana–Champaign, Urbana, IL 61801-2918 USA (e-mail: park35@gmail.com).

N. Kim is with the Department of Mechanical Science and Engineering, University of Illinois at Urbana–Champaign, Urbana, IL 61801-2906 USA (e-mail: kim847@illinois.edu).

D. T. Morisette was with the Department of Electrical and Computer Engineering, and also with Micro and Nanotechnology Laboratory, University of Illinois at Urbana–Champaign, Urbana, IL 61801-2918 USA. He is now with Group 4 Development, LLC, West Lafayette, IN 47906-1157 USA (e-mail: dtmorisette@gmail.com).

N. R. Aluru is with the Department of Mechanical Science and Engineering, the Beckman Institute for Advanced Science and Technology, the Department of Electrical and Computer Engineering, and the Bioengineering Department, University of Illinois at Urbana–Champaign, Urbana, IL 61801-2906 USA (e-mail: aluru@uiuc.edu).

R. Bashir is with the Department of Electrical and Computer Engineering, the Department of Bioengineering, the Department of Mechanical Science and Engineering, and the Micro and Nanotechnology Laboratory, University of Illinois at Urbana–Champaign, Urbana, IL 61801-2918 USA (e-mail: rbashir@illinois.edu).

Color versions of one or more of the figures in this paper are available online at http://ieeexplore.ieee.org.

Digital Object Identifier 10.1109/JMEMS.2012.2189359

I. Introduction

A microelectromechanical systems (MEMS)-based resonant mass sensor can be an ideal tool to measure the mass of micro- and nanosized particles and to characterize various physical processes at the micro- and nanoscales. The sensor measures a shift in the resonance frequency of the structure before and after the attachment of a target entity, where the shift in the resonant frequency can be used to calculate the mass of the target entity. Due to their high sensitivity and small dimension, MEMS-based resonant mass sensors have been extensively studied as biological and chemical sensors [1], [2]. Resonant cantilever mass sensors have been used to measure the mass of bacteria and single virus in air [3], [4] and *Bacillus anthracis* Sterne spores in liquid [5]. Monitoring of the growth of *Escherichia coli* [6], fungus [7], [8], and adherent single mammalian cells [9] immobilized on the MEMS mass sensors has also been reported. An innovative design involving a cantilever-shaped hollow microchannel resonator with high mass sensitivity [10] has also been used to measure the growth rate of a population of suspended single cells [11].

One of the most common and intriguing microscaled physical processes is the evaporation of fluid and droplets. A small droplet of liquid in air evaporates over time as its mass and the surface area decrease simultaneously. The evaporation rate can be affected by various factors, such as the vapor pressure and the enthalpy of evaporation of the liquid, the surface area of the microdroplets, the ambient temperature, and the liquid's vapor concentration in air. Understanding the detailed mechanisms of the microdroplet evaporation is important due to the widespread use of microdroplets in various applications, such as semiconductor surface cleaning [12]–[14], ink-jet printing [15], [16], and self-assembly [17], [18]. For example, evaporating droplets were used to elongate and fix deoxyribonucleic acid (DNA) molecules to charged surfaces [17]. Chopra *et al.* [18] also presented an experimental and computational investigation of orienting and stretching of DNA molecules inside evaporating droplets. Using various experimental methods, important insights have been gained regarding several aspects of evaporation process such as hydrodynamic flow inside of a droplet [19]–[21], effects of the thermal conductivity of the substrate [22], and the vapor diffusion at the droplet surface [23]. However, direct measurement of mass changes during evaporation of microdroplets has not been reported.

A MEMS mass sensor can be a good candidate for monitoring the microdroplet evaporation process, but there are a few challenges to be overcome. First, the mass distribution of the microdroplet is changing during the process of evaporation.

The mass sensitivity of the conventional cantilever mass sensor changes from zero to its maximum value, as the mass moves from the fixed end to the free end [24], [25]. Therefore, conventional MEMS mass sensors based on cantilever geometry cannot accurately monitor the evaporation process, due to this spatially nonuniform mass sensitivity. Second, depending on the vapor pressure of the target fluid, the microdroplet can evaporate completely in a fraction of a second, and the sampling rate of the mass measurement should be high enough to capture the dynamics of the evaporation process.

Here, we report the use of a MEMS resonant mass sensor with a uniform mass sensitivity for monitoring the evaporation process of microdroplets of water and dimethyl sulfoxide (DMSO). By feeding back the sensor velocity to the actuation signal, the sensor was kept in self-oscillation to achieve high sampling rate of the mass measurement. Theoretical analysis and parametric optimization of the sensor structure for uniform mass sensitivity are discussed in Section II. Electromagnetic actuation and feedback circuit for self-oscillation are presented in Section III. Section IV contains the experimental result of the evaporation process of water and DMSO microdroplets in air.

II. Sensor Design

A. Mass Sensitivity and Design Strategy

The mass sensitivity of a MEMS resonant mass sensor can be defined as the ratio of the resonant frequency shift to the added mass attached to the sensor. At resonance, the time average kinetic energy of the resonant mass sensor and the added mass should be the same as the time average strain energy [25]. The total kinetic energy is

$$E_{\mathrm{Kin\_total}} = E_{\mathrm{Kin,sensor}} + E_{\mathrm{Kin},\Delta m} = \frac{1}{2} m_0 a_n^2 \omega_{n+\Delta m}^2 + \frac{1}{2} \Delta m \omega_{n+\Delta m}^2 a_n^2 U_n^2(z_{\Delta m}) \quad (1)$$

where m_0 is the effective mass of the sensor, a_n is the modal amplitude at the nth mode, $\omega_{n+\Delta m}$ is the resonant frequency of a loaded sensor, Δm is the added mass, $U_n(z)$ is the time-independent mode shape, and $z_{\Delta m}$ is the location of the added mass [25].

If we assume that the resonant mode shape is not changed due to the relatively small added mass, the strain energy is the same as the kinetic energy of the unloaded sensor. Then, the time average strain energy is

$$E_{\mathrm{strain}} \approx \frac{1}{2} m_0 a_n^2 \omega_n^2 \quad (2)$$

where ω_n is the resonant frequency of the unloaded sensor. By equating (1) and (2) and assuming that the frequency shift is relatively small, the mass sensitivity of the resonant mass sensor can be described as

$$\frac{\Delta\omega}{\Delta m} = \frac{\omega_n - \omega_{n+\Delta m}}{\Delta m} = \frac{\omega_{n+\Delta m}^2 U_n^2(z_{\Delta m})}{m_0(\omega_n + \omega_{n+\Delta m})} \approx \frac{\omega_n}{2m_0} U_n^2(z_{\Delta m}) \quad (3)$$

where $\Delta\omega$ is the frequency shift due to the added mass.

From the aforementioned equation, the mass sensitivity of the sensor is directly related to the square of the sensor deflection $U_n(z_{\Delta m})$ where the added mass is attached.

The variation of the mass sensitivity or the ratio of the maximum mass sensitivity to the minimum mass sensitivity on the target attachment site can be defined as follows:

$$\Delta S = \frac{\left(\frac{\Delta\omega}{\Delta m}\right)_{\max} - \left(\frac{\Delta\omega}{\Delta m}\right)_{\min}}{\left(\frac{\Delta\omega}{\Delta m}\right)_{\max}} = \frac{\left(U_n^2(z)\right)_{\max} - \left(U_n^2(z)\right)_{\min}}{\left(U_n^2(z_{\Delta m})\right)_{\max}} = \frac{U_{\max}^2 - U_{\min}^2}{U_{\max}^2} \quad (4)$$

where $U_{\max}$ and $U_{\min}$ are the maximum and the minimum displacement of the target attachment site on resonance, respectively. Therefore, to keep the mass sensitivity of the resonant mass sensor uniform, the modal deflection of the target attachment site at its resonance should be forced to be constant over the target attachment site.

For quantitative investigation of the modal deflection of a specific geometry, modal analysis was performed with ANSYS, based on the following governing equation:

$$[M]\{\ddot{u}\} + [K]\{u\} = \{0\}, \qquad \text{where } \{u\} = \{\phi\}_i \cos\omega_i t \quad (5)$$

$$\left|[K] - \omega^2[M]\right| = 0, \qquad \text{where } \omega = 2\pi f \quad (6)$$

where M, k, u, ϕ, and f are the structural mass matrix, structural stiffness matrix, nodal displacement vector, eigenvector of modal shape, and resonant frequency, respectively.

One of the most straightforward strategies to maintain spatially uniform deflections of the target attachment site is to use a double-clamped beam structure and place the target attachment site or the platform in the center. Also, by making the target attachment site wider and thicker, the variation of deflection can be further reduced. The structure in Fig. 1(a) is an example of this approach. As can be seen in the figure, there is a single global deflection maximum formed at the center of the platform. Since the flexural bending of the spring is directly delivered to the platform, the bending forces from each spring get centralized, producing a single global deflection maximum. This global deflection maximum leads to a larger deflection variance and makes the mass sensitivity less uniform. The scale bars in Fig. 1 are the displacement amplitude of the sensor structures in resonance. The mass sensitivity variation is calculated to be 5.87% $(= (220\,755^2 - 214\,175^2)/220\,755^2)$ based on (4) and Fig. 1(a). The scale bars are in arbitrary units.

To avoid the concentration of flexural bending forces and the formation of a global deflection maximum point on the target attachment site, the direct transfer of the flexural bending force from the springs to the platform should be minimized. One way to reduce the transfer of the flexural bending is to convert the flexural bending into torsional force to produce well-distributed local maximum deflection points, instead of a centralized global maximum deflection point. Fig. 1(b) shows the "four-folded-spring structure" which is composed of the platform for the target attachment site and four fully folded springs. Fig. 1(c) shows the deflection of the torsional spring marked with a dotted circle in Fig. 1(b), clearly showing the torsional deflection. As a result, part of the flexural bending force from the springs is converted to twisting torque by the torsional springs before it is

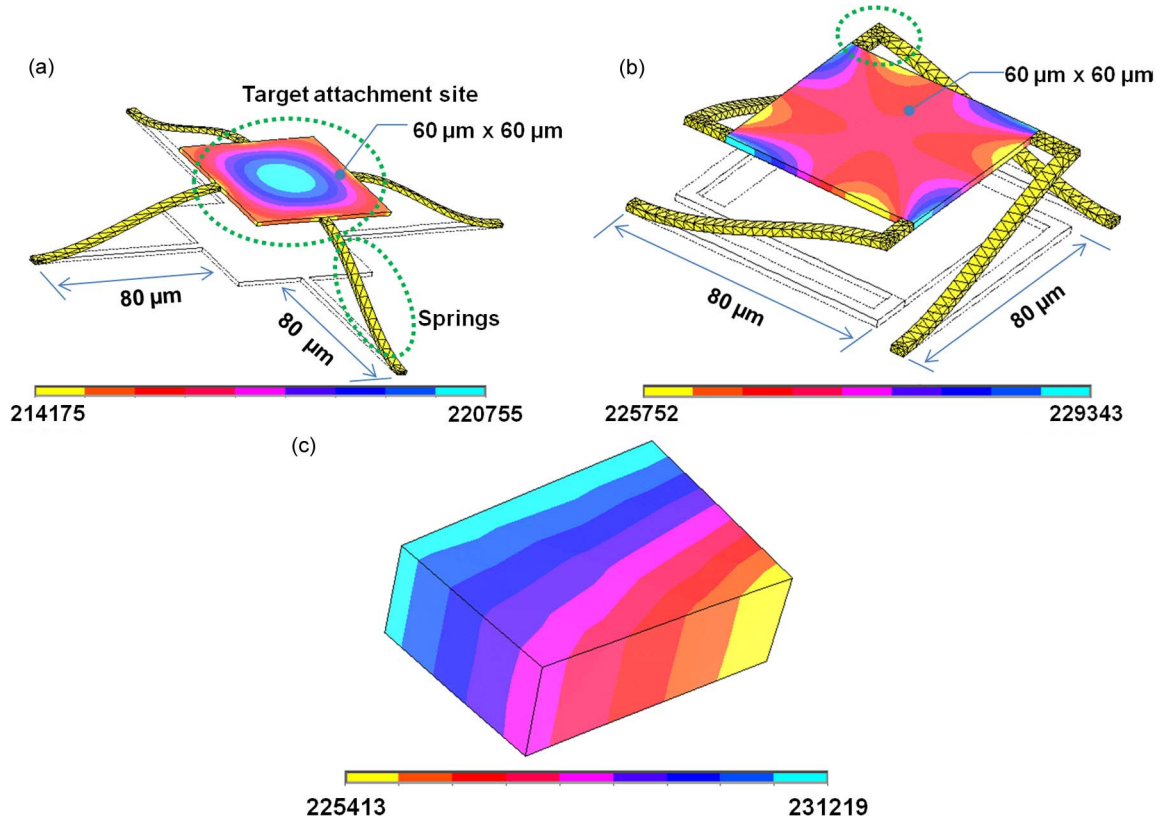

Fig. 1. FEA showing the displacement magnitude on resonance. (Meshed area) Springs are 4 μm wide and 2 μm thick. The target attachment sites are superimposed with contour plots showing the displacement magnitude on resonance. (a) Mass sensor structures without conversion of flexural bending into torsional bending. (b) Mass sensor structure with conversion of flexural bending into torsional bending. (c) Close-up of torsional bending of the spring, which is indicated with a dotted circle in (b).

transferred to the platform. Therefore, instead of a centralized maximum deflection, the deflection of the platform is well distributed along the edges, leaving the deflection of most of the area uniform, as can be seen in Fig. 1(b). The variation of the mass sensitivity of the structure with four fully folded springs is 3.11% $(= (229\,343^2 - 225\,752^2)/229\,343^2)$, where 229 343 and 225 752 are the maximum and the minimum displacement of the target attachment site in resonance from the scale bar in Fig. 1(b).

B. Parametric Studies of Structural Dimension for Uniform Sensitivity

The effect of the dimensional parameters of the sensor structure on the uniformity of the mass sensitivity is further analyzed with numerical analysis. In this analysis, the "four-folded-spring structure" is used, and three key structural parameters, namely, L, d, and θ, as shown in Fig. 2(a), are varied. L, d, and θ are the length of the torsional springs, the position of the springs with respect to the center of the platform, and the angle of the flexural springs, respectively. In Fig. 2(b) and (c), modal simulations of the sensor structures with varying dimensions are performed with ANSYS, which is similar to that in Fig. 1. Then, the maximum and minimum displacement magnitudes of the target attachment site are extracted from the scale bar to calculate the variation of the mass sensitivity, using (4). Fig. 2(b) shows the variation of the mass sensitivity of the sensor, with varying L and θ. The spring position is set to zero. In Fig. 2(c), the spring length L is set to 10 μm, and the position of the springs is varied with different spring angles θ. Based on Fig. 2(c), the uniformity of the mass sensitivity is optimal when the leg angle is zero and the spring position is around 4 μm. However, in this work, the leg angle and the leg position are set to 45° and 0 μm, respectively, due to challenges in the fabrication, as described in the following section. The modal shape of the sensor used in this paper is shown in Fig. 2(d), and its variation of the mass sensitivity is calculated to be 4.06% $(= (230\,732^2 - 225\,996^2)/230\,732^2)$. From the modal simulation, the resonant frequency and the spring constant are 182 kHz and 21.6 N/m, respectively.

III. Self-Oscillation System for Rapid Frequency Measurement

A. Measurement Setup for Electromagnetic Actuation

The layout of an individual sensor is shown in Fig. 3(a). Using reactive-ion etching, the sensor structures are defined on the 2-μm-thick device layer of a silicon-on-insulator (SOI) wafer. Then, the bulk silicon beneath the sensor structure is removed as a sacrificial layer, using isotropic dry etching with xenon difluoride (XeF_2) in gas phase through the release windows in Fig. 3(a). The placement of the release windows is critical to maximize the depth of the cavity beneath the platform, while minimizing the etch undercut beneath the base of the spring. For this reason, the release windows are kept at 60 μm away from the base of the spring, while placing them as close to the

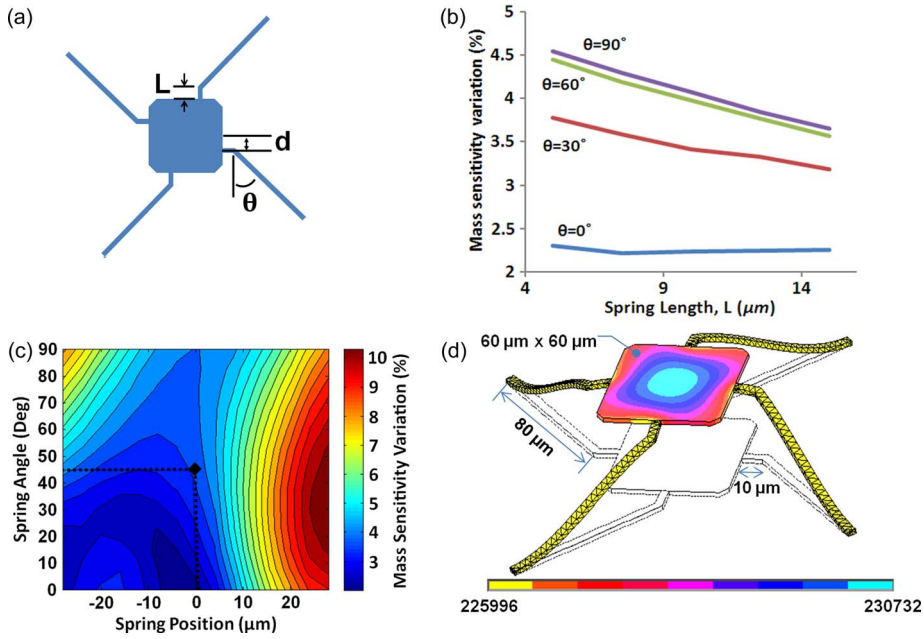

Fig. 2. Numerical analysis to optimize the sensor structure. (a) Schematic showing the variables to be optimized for the uniform mass sensitivity. (b) Variation of the mass sensitivity with varying spring angle (θ) and spring length (L) using the step size of $30°/1$ μm. (c) Two-dimensional contour plot of variation of mass sensitivity on the target attachment site, with varying spring angle (θ) and spring position (d) using the step size of $10°/4$ μm. The dimension of the sensor used in this study is pointed with a black dot at $\theta = 45°$ and $d = 0$. (d) Dimensions and modal analysis of the sensor used in this study.

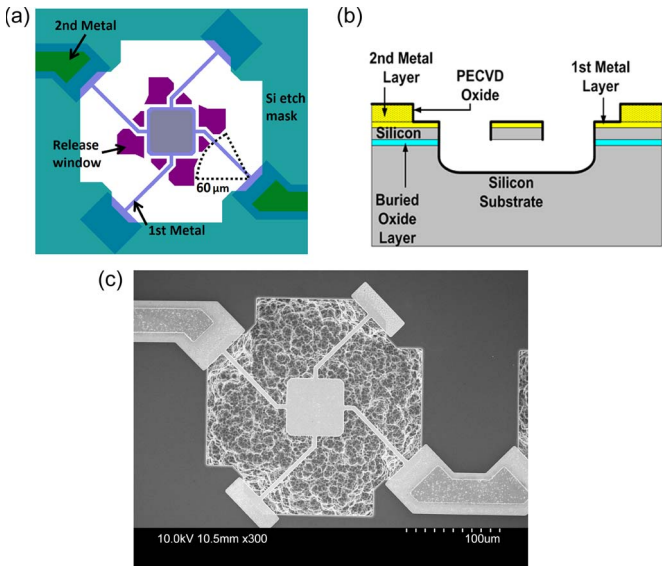

Fig. 3. (a) Layout of an individual sensor. (b) Cross-sectional diagram of the sensor. (c) Top-view SEM image of the fabricated sensor.

platform as possible. This approach ensures the platform to be released much earlier than the springs, making enough space between the platform and the bottom of the cavity beneath the released structure. However, to provide available space for the release window close to the platform, the leg angle is chosen to be 45°, which leads to a slight degradation of the uniformity of the mass sensitivity. The cross-sectional view of the sensor is shown in Fig. 3(b). The suspended platform and springs have a 100-nm silicon dioxide layer as the insulator, a 50-nm gold and 20-nm chromium layer as the current path, and a 2-μm silicon layer as the mechanical structure. Fig. 3(c) shows the scanning electron micrograph (SEM) images of the completed sensor. Detailed information on the fabrication process of the device can be found in an earlier report [9].

The measurement setup is shown in Fig. 4(a). The sensor is actuated with an electromagnetic force. The sensor is placed in the uniform magnetic field generated by the permanent magnet. A sinusoidal actuation current is passing through the platform and the springs. With an externally applied constant transverse magnetic field, Lorentz force is induced to actuate the sensor in the vertical direction. The velocity of the sensor is measured by a laser Doppler vibrometer (LDV) (MSV-300, Polytec, USA). Since the movement of the sensor platform is mainly a vertical translation involving minimal flexural bending, the velocity or the displacement of the platform cannot be measured with conventional atomic force microscopy setups, in which only the deflected angle of the structure can be measured. The velocity output from the LDV is analyzed with a lock-in amplifier (Model 7280, Signal Recovery, USA), to produce the magnitude and the phase information of the velocity with respect to the actuation current.

The externally applied magnetic field should be uniform and strong enough to induce a Lorentz force large enough to actuate the sensor. Moreover, the magnetic field should be perpendicular to the current flow. For these reasons, a nickel alloy magnetic core is used to hold two N52 grade rare earth magnets about 1-cm distance apart from each other, generating uniform magnetic fields. From the finite-element analysis (FEA), the magnetic field flux experienced by the device is around 0.4 T. To confirm the linearity of the electromagnetic actuation, the pseudostatic deflection of the sensor is measured with a sinusoidal actuation voltage at 10 kHz, which is much lower than the experimentally measured resonant frequency of 160 kHz. Fig. 4(b) shows the deflection of the sensor with respect to the applied actuation current.

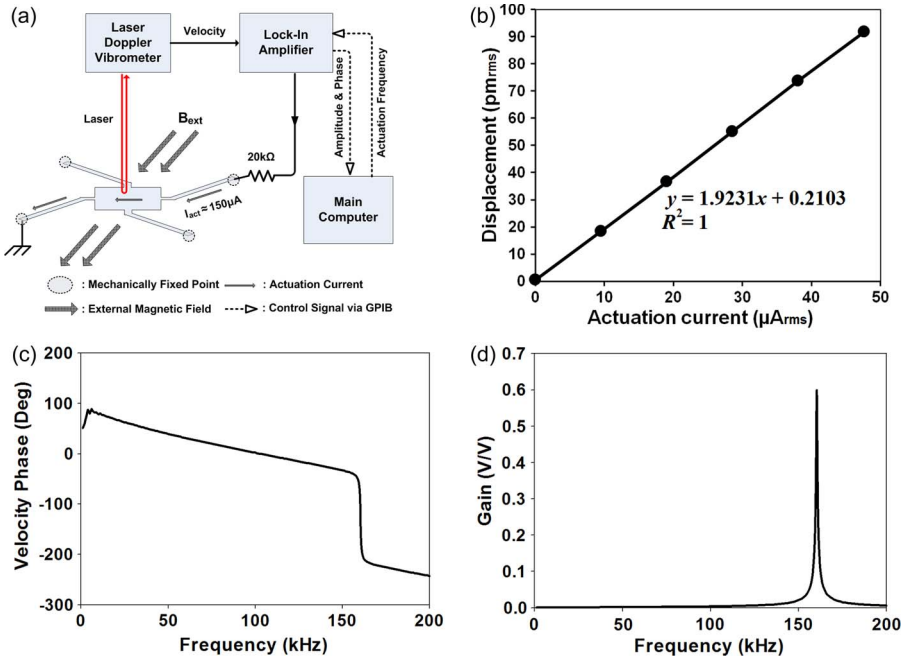

Fig. 4. (a) Experimental setup for the sensor characterization using an LDV. (b) Displacement of the sensor as it is quasi-statically driven with the actuation current at 10 kHz. (c) Phase and (d) gain of the sensor and the LDV system.

Finally, the frequency response $G(j\omega)$ of the sensor and the LDV is measured in air. The typical frequency response of the device is shown in Fig. 4(c) and (d). The slope of the phase is due to the internal time delay ($\sim$1.9 μs) of the LDV's velocity decoder for the signal processing. The resonant frequency and the quality factor in Fig. 4(c) and (d) are measured to be 160.4 kHz and 216.7, respectively. The sensor can be modeled as a second-order-harmonic oscillator with a mass of 16.6 ng, a damping coefficient of 77.3 nN$\cdot$s/m, and a spring constant of 16.9 N/m.

B. Feedback Circuit for Self-Oscillation

In an earlier report [9], the resonant frequency of the sensor in liquid was determined based on the repeatedly measured value of the velocity phase to enhance the accuracy of the mass measurement. However, this approach requires large number of samples of the phase to suppress the noise and takes about 60 s to complete the resonant frequency measurement, which is not suitable for rapidly evaporating microdroplets.

For the measurement of microdroplet evaporation, the sensor is kept self-oscillating at its resonant frequency by providing a feedback of the sensor velocity signal to the sensor actuation current, as shown in Fig. 5(a). The resonant frequency of the sensor can be directly measured from the oscillating signal, either by using a frequency counter (34401A, Agilent, USA) or by recording the signal with a digital oscilloscope (DSO8064A, Agilent) with an upgraded memory option (64 million points per channel). The former is used for slowly evaporating DMSO microdroplets, and the latter is used for rapidly evaporating water microdroplets. The sensor velocity is detected with LDV, and the velocity signal is fed back to the sensor actuation current through the feedback circuit. The feedback circuit amplifies the signal and shifts the phase of the signal, so that the combined system oscillates at the resonant frequency of the sensor. The schematic of the feedback circuit is shown in Fig. 5(b). The first stage is a dc-blocked noninverting amplifier with a fixed gain. The second stage is an all-pass filter for phase shifting. It has a unit gain and a varying phase response of $\angle H(j\varpi) = 180 - 2\arctan(\varpi RC)$, where C is fixed to 1 nF and R can be increased up to 11 kΩ. The third stage is a noninverting amplifier with a variable gain, which can be adjusted with two varying resistors. The frequency response of the feedback circuit $H(j\omega)$ is shown in Fig. 5(c).

When $H(j\omega) * G(j\omega) \geq 1$ and $\angle[H(j\omega) * G(j\omega)] = 2n\pi$, the system starts self-oscillation at the resonant frequency of the sensor. In Fig. 5(d), the phase of the feedback circuit and the inverse of the phase of the sensor and the LDV system are shown. The two phase curves intersect each other near the resonant frequency of the sensor, where there is a sharp shift of the phase of the sensor and the LDV system. For a given phase and gain setting of the feedback circuit, there is a minimum resonant frequency of the sensor $f_{\min}$, below which the aforementioned self-oscillation condition cannot be satisfied.

The instantaneous mass of the microdroplet on the sensor $m(t)$ is obtained with the following equation:

$$m(t) = \frac{k_0}{4\pi^2}\left(\frac{1}{f_r^2(t)} - \frac{1}{f_0^2}\right) \tag{7}$$

where f_0, k_0, and $f_r(t)$ are the resonant frequency of the sensor itself, the spring constant of the sensor, and the measured instantaneous resonant frequency, respectively.

Since the majority of the effective mass is concentrated on the center rectangular platform, the spring constant k_0 was obtained with the following equation:

$$k_0 = 4\pi^2 * f_0^2 * m_{\text{platform}} \tag{8}$$

where m_{platform} is the mass of the platform, calculated from the dimension and the density of the silicon.

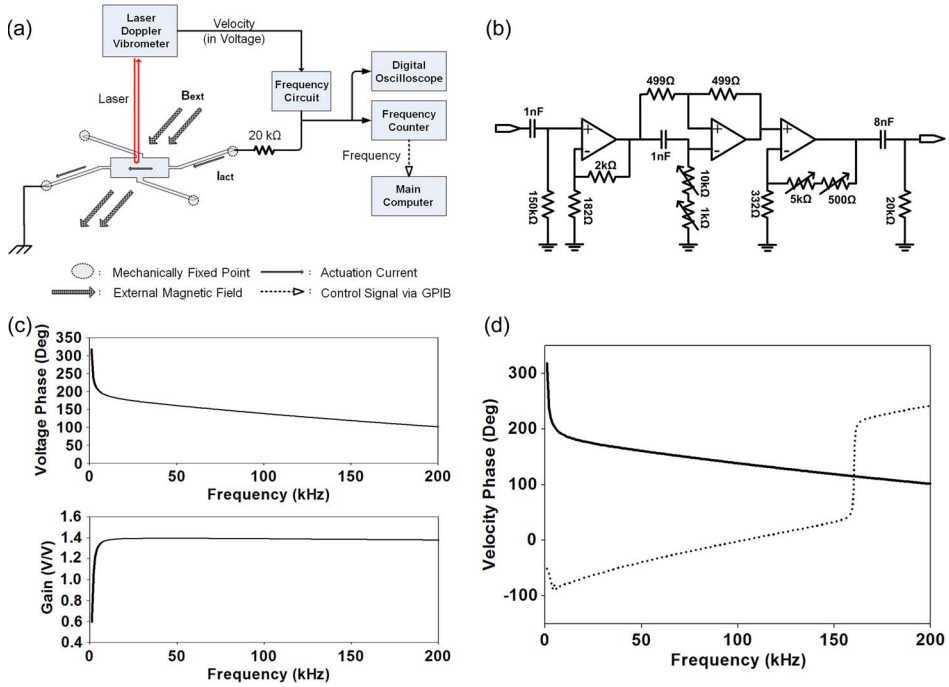

Fig. 5. (a) Experimental setup for the self-oscillation of the sensor. (b) Schematic diagram of the feedback circuit. (c) Gain and phase of the feedback circuit. (d) (Solid line) Phase of the feedback circuit and (dotted line) the inversed phase of the sensor and the LDV system.

IV. Experimental Result

A. Measurement of Mass of Evaporating Microdroplet

The microdroplets are deposited using a cell microinjector (IM300, Narishige Group, Japan). The microcapillary holder of the microinjector is attached to a motorized micromanipulator. After attaching a microcapillary (Sterile TransferTips-RP, Effendorf) to the holder, the end of the microcapillary is immersed in the desired liquid, and the sample liquid is pulled into the microcapillary by applying negative pressure with the cell microinjector. After loading the sample liquid, the end of the microcapillary is brought into close proximity of the mass sensor with the micromanipulator (HS3-6M/World Precision Instruments). Prior to each experiment, the sensor is treated with 2 min of oxygen plasma to enhance the hydrophilicity of the sensor surface. By applying a short pulse ($\sim$20 ms) of positive pressure, a small amount (20–30 ng) of the sample liquid is deposited on the mass sensor. The temperature of the sensor device is controlled with a heating element integrated into the custom-made printed circuit board (PCB) and a thermistor attached to the sensor device. Also, to avoid local concentration of the vapor of the sample liquid, an airflow of 8–10 sccm is applied to the sensor through a small tubing, which was attached to the PCB.

The output voltage of the feedback circuit is recorded directly after deposition of the microdroplet on the sensor. Initially, the resonant frequency of the sensor with the microdroplet is shifted much lower than the minimum resonant frequency necessary for the stable self-oscillation $f_{\min}$, so that the system does not start self-oscillation. However, as the microdroplet evaporates, the resonant frequency of the sensor with the microdroplet becomes larger than $f_{\min}$, and the combined system oscillates by itself at the resonant frequency of the sensor with the microdroplet. Once the system starts self-oscillation, the resonant frequency of the sensor can be stably obtained from the waveform. After the microdroplet has completely evaporated, the combined system self-oscillates at the resonant frequency of the sensor itself.

During self-oscillation, the output voltage from the feedback circuit is $\pm$4-V sawtooth wave at about 160 kHz. The resistance of the actuation current path on nine sensors in a single row is measured to be 1.179 kΩ ($Std = \pm 6.9\ \Omega$). Since most of the potential difference is applied across a 20-kΩ resistor, which was serially connected to the device, as shown in Fig. 5(a), the heat generated by the finite conductance of the current path of a single sensor is calculated to be less than 1.56 μW. With a simple estimation of the heat conductance of the four springs, the temperature rise due to the ohmic heating is less than 61 mK, owing to high thermal conductivity of silicon.

The dark-field microscopy of the evaporating DMSO microdroplet on the sensor in ambient environment is shown in Fig. 6(a), with the time stamps and the extracted mass indicated below the images. Due to the surface tension, the microdroplet initially looks similar to a half sphere. As the microdroplet evaporates, its volume decreases, and the surface becomes flat. Then, as most of the microdroplet evaporates, small defects on the sensor surface can be seen. The mass decrease rates of DMSO and water microdroplets were measured at different temperatures, as shown in Fig. 6(b) and (c), respectively. The masses of DMSO microdroplets and water microdroplets were measured every 150 ms for DMSO and 5 ms for water. At each temperature, the measurements were repeated multiple times. For both DMSO and water, the mass of the microdroplet decreased at constant rate initially, and then, as most of the microdroplet evaporates, the rate of the mass decrease was only slightly reduced.

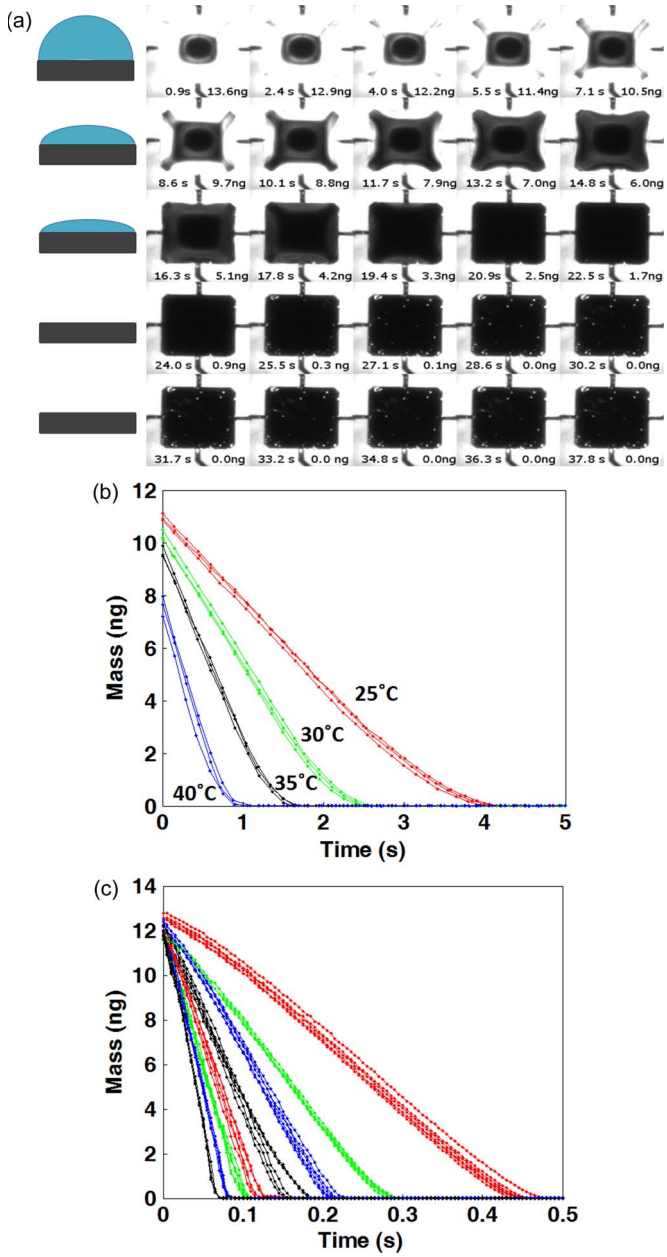

Fig. 6. (a) Time-lapsed images of the evaporating DMSO microdroplet. Column on the left shows a drawn cross-sectional schematic of the droplet on the pedestal. (b) Typical results of mass decrease of the evaporating DMSO microdroplet at different temperatures. (c) Typical mass decrease pattern of the evaporating deionized (DI) water microdroplet at different temperatures ($T = 25$ °C (rightmost curve in red), 30 °C, 35 °C, 40 °C, 45 °C, 50 °C, 55 °C, and 60 °C).

B. Evaporation Rate Based on the Surface Area From FEA

To further investigate the evaporation rate or the rate of mass decrease per unit area of the microdroplet surface, the surface area of the microdroplet at each mass point is necessary. A full 3-D FEA is performed with COMSOL Multiphysics to determine the surface area of the microdroplets with six different volumes within the range of experiment data. The droplet shape of a finite volume under surface tension is obtained to calculate the surface area of the droplet. Only a quarter of the droplet is simulated based on the symmetry of the structure. The

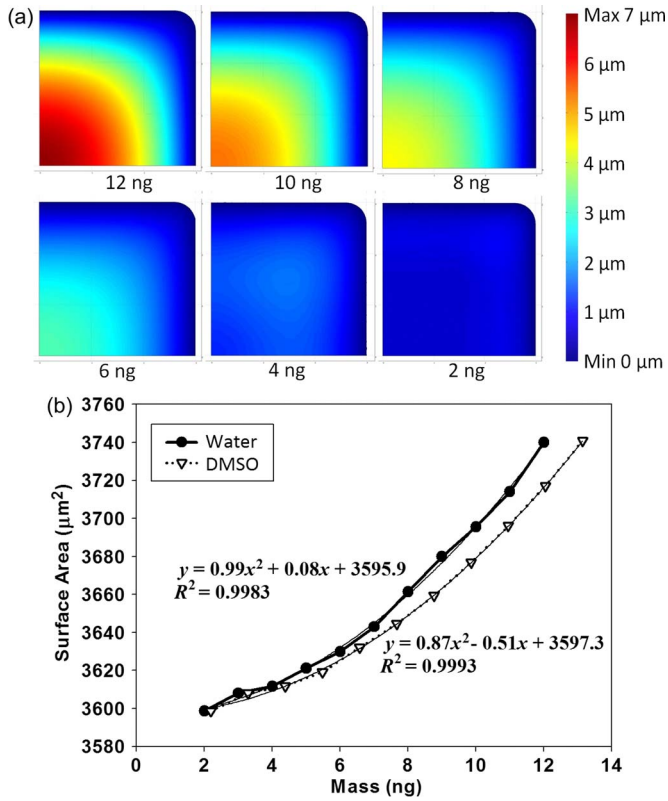

Fig. 7. (a) Two-dimensional top-view simulation results of the droplet (one-fourth segment) for different droplet mass values. The color scale shows the height of the droplet from the converged solution of the 3-D FEA. (b) Simulated surface area of the water and the DMSO microdroplet for different mass values.

incompressible Navier–Stokes equations are used to model the droplet deformation

$$\rho\left(\frac{\partial \mathbf{u}}{\partial t}+\mathbf{u}\cdot\nabla\mathbf{u}\right)-\nabla\cdot\left(\eta\left(\nabla\mathbf{u}+(\nabla\mathbf{u})^{T}\right)\right)+\nabla p=\mathbf{F} \quad (9)$$

$$\nabla\cdot\mathbf{u}=0 \quad (10)$$

where η is the dynamic viscosity, ρ is the density, $\mathbf{u}$ is the velocity, p is the pressure, and $\mathbf{F}$ is the body force due to gravity.

The bottom of the droplet is fixed, modeling a pinned radius. Symmetric boundary condition is used along the axis of symmetry, and all other surfaces are treated as free boundaries on which the surface tension acts. The arbitrary Lagrangian–Eulerian method is used to modify the shape of the mesh accounting for the physical deformation. In the presence of surface tension, the free boundary condition is given by

$$\left(-p\mathbf{I}+\eta\left(\nabla\mathbf{u}+(\nabla\mathbf{u})^{T}\right)\right)\mathbf{n}=-P_a\mathbf{n}+\Gamma\gamma\mathbf{n} \quad (11)$$

where $\mathbf{n}$ is the outward unit normal vector, P_a is the surrounding pressure (atmospheric pressure in this model), Γ is the mean curvature of the interface, and γ is the surface tension which is assumed to be constant. The surface areas obtained via these simulations are used in later analyses to calculate the evaporation rate.

Fig. 7(a) shows the simulated shape of the microdroplet on the sensor surface. In Fig. 7(b), the surface areas of DMSO and water are fitted to a second-order polynomial. The surface area of the DMSO was slightly higher than that of water.

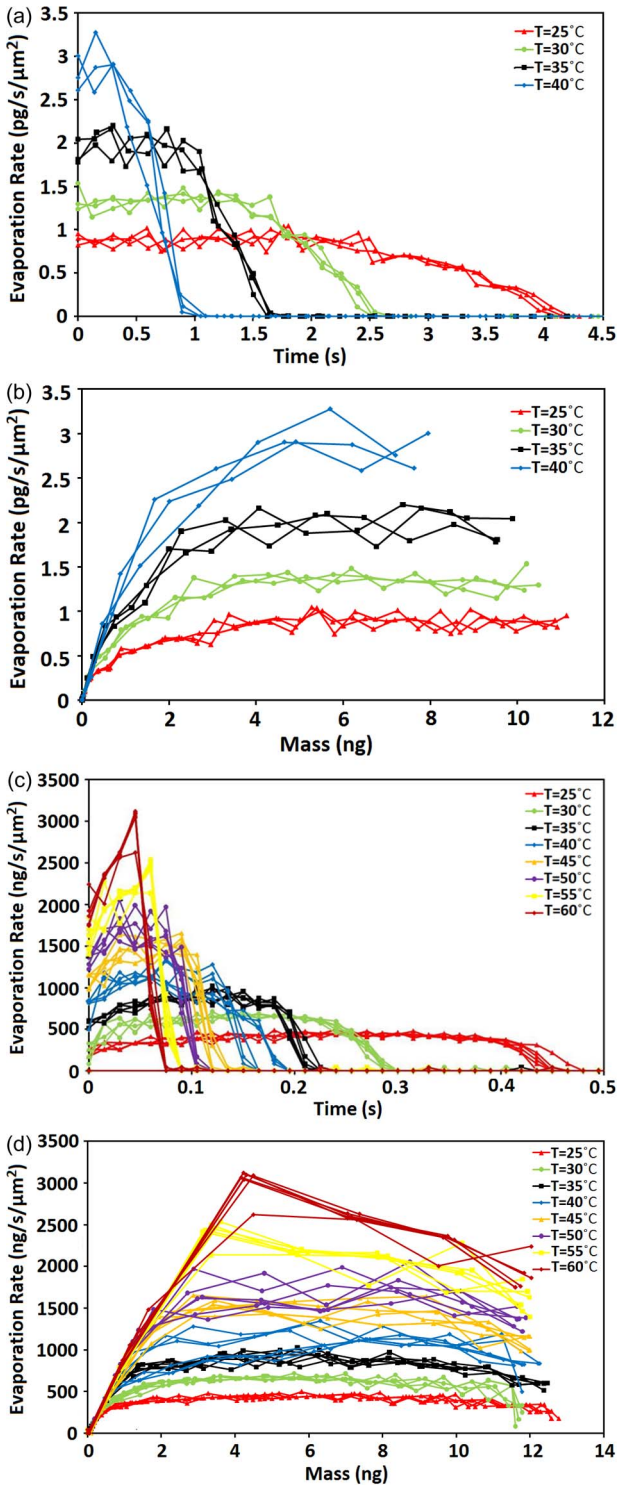

Fig. 8. (a) Instantaneous evaporation rate of DMSO microdroplet versus time at different temperatures, (b) instantaneous evaporation rate of DMSO versus the droplet mass at different temperatures, (c) instantaneous evaporation rate of water versus time at different temperatures, and (d) instantaneous evaporation rate of water versus the droplet mass at different temperatures.

By dividing the rate of mass decrease by the surface area of the microdroplet, the evaporation rate per unit area can be obtained, as shown in Fig. 8(a) and (c) for DMSO and water, respectively. For both cases, the evaporation rates seem to be roughly constant initially and then decrease when most of the droplet is evaporated. Fig. 8(b) and (d) shows the evaporation rate with respect to the mass of the microdroplet and that the evaporation rates decrease when the mass of the microdroplet is lower than ∼2 ng or the average height of the microdroplet becomes smaller than ∼560 nm.

C. Extraction of the Enthalpy of Vaporization

Enthalpy of vaporization or enthalpy of evaporation is one of the fundamental properties of a liquid, and it is defined as the energy required to evaporate a certain amount of the liquid into gas at atmospheric pressure. From the measured evaporation rate of the microdroplet at different temperatures, the enthalpy of vaporization can be obtained by the Clausius–Clapeyron relation as shown in the following:

$$\ln P = -\frac{\Delta h}{R}\frac{1}{T} + C \tag{12}$$

where P, Δh, R, T, and C are the vapor pressure, the enthalpy of vaporization, the gas constant, the temperature (in kelvins), and an arbitrary constant, respectively.

The evaporation rate R_{evap} is proportional to the vapor pressure

$$\ln P = \ln R_{\text{evap}} + C_1 = -\frac{\Delta h}{R}\frac{1}{T} + C$$
$$\ln R_{\text{evap}} = -\frac{\Delta h}{R}\frac{1}{T} + C - C_1 = -\frac{\Delta h}{R}\frac{1}{T} + C_2. \tag{13}$$

To exclude the decreased evaporation rate with the microdroplet mass smaller than ∼2 ng, the average evaporation rate is obtained by measuring the time duration, in which the droplet mass is decreased from 11 to 4 ng for DMSO and from 10 to 3 ng for water. The evaporation rates of water and DMSO at various temperatures are shown in Fig. 9(a) and (b), respectively. To extract Δh for each liquid, the log value of the evaporation rates is plotted with respect to the inverse of the temperature, as shown in Fig. 9(c) and (d). The log value of the evaporation rate can be approximated with a straight line, which is consistent with (13). The enthalpy of vaporization Δh is obtained from the slope of the plot, which is $-\Delta h/R$. The obtained Δh values for water and DMSO are presented in Table I, which is close to the literature values of 40.65 kJ/mol [26] and 52.9 kJ/mol [27], [28] for water and DMSO, respectively.

V. Conclusion

In this work, a MEMS mass sensor with uniform mass sensitivity and electromagnetic actuation was used to measure the evaporation rate of the microdroplet of water and DMSO. The sensor was fabricated on SOI wafers using standard microfabrication process. The effects of the structural parameters on the variation of the mass sensitivity were quantitatively investigated. The sensor is electromagnetically actuated with Lorentz force, and its motion was detected with a laser. A rapid mass determination method was devised based on self-oscillation of the mass sensor to measure rapidly changing resonant frequency of the sensor with a microdroplet in real time. The evaporation rates of water and DMSO at various temperatures were measured to determine the enthalpy of vaporization of the liquids. We believe that the developed sensor

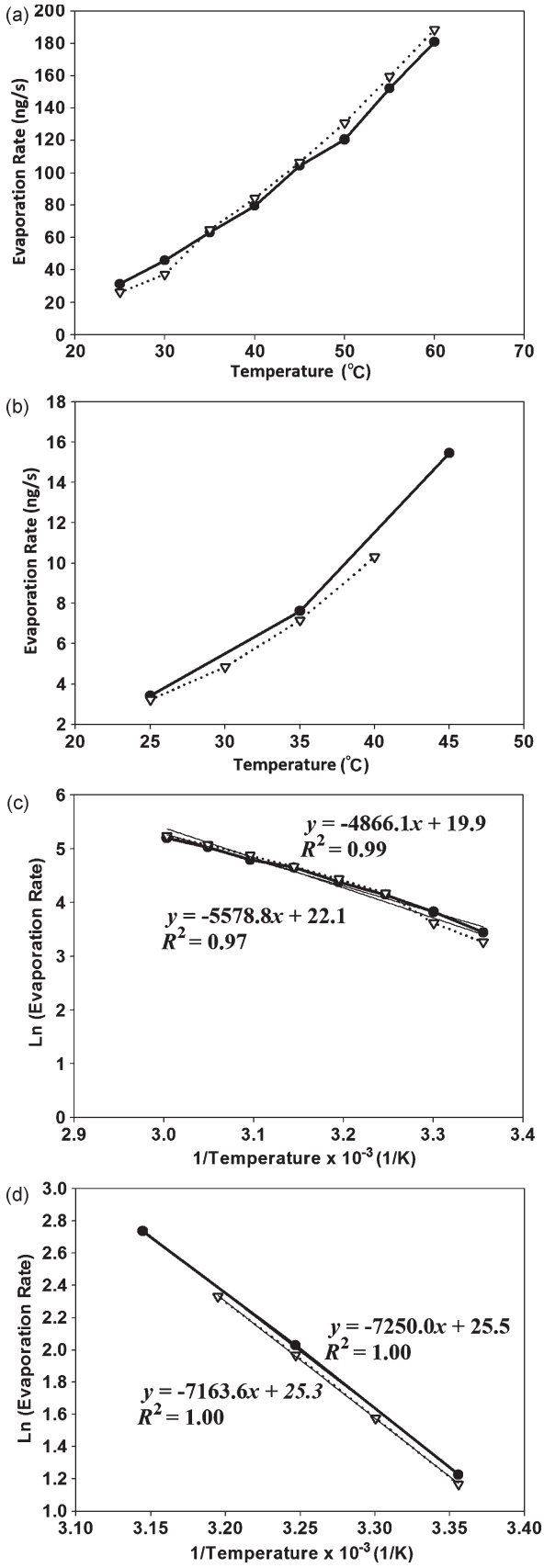

Fig. 9. Evaporation rate of each sample is measured twice and shown in the dashed and solid lines. (a and c) Evaporation rate of the DI water microdroplet versus temperature. (b and d) Evaporation rate of the DMSO microdroplet versus temperature.

TABLE I
ENTHALPY OF VAPORIZATION VALUES REPORTED IN THE LITERATURE AND THE MEASURED VALUES FROM OUR EXPERIMENTS

	Measured Enthalpy of Evaporation (kJ/mol)	Values from Literature [26-28]
DMSO	Exp. 1: 60.3 Exp. 2: 59.6	52.9
DI water	Exp. 1: 40.5 Exp. 2: 46.4	40.65

can be a valuable tool to elucidate various microscaled physical processes and biological phenomena involving evaporation and mass transport.

ACKNOWLEDGMENT

The authors would like to thank the staff of the Micro and Nanotechnology Laboratory at the University of Illinois at Urbana–Champaign for the assistance in device fabrication.

REFERENCES

[1] H. Craighead, "Nanomechanical systems—Measuring more than mass," *Nat. Nanotechnol.*, vol. 2, no. 1, pp. 18–19, Jan. 2007.
[2] P. S. Waggoner and H. G. Craighead, "Micro- and nanomechanical sensors for environmental, chemical, and biological detection," *Lab Chip*, vol. 7, no. 10, pp. 1238–1255, Oct. 2007.
[3] A. K. Gupta, D. Akin, and R. Bashir, "Detection of bacterial cells and antibodies using surface micromachined thin silicon cantilever resonators," *J. Vac. Sci. Technol. B, Microelectron. Nanometer Struct.*, vol. 22, no. 6, pp. 2785–2791, Nov. 2004.
[4] A. K. Gupta, D. Akin, and R. Bashir, "Single virus particle mass detection using microresonators with nanoscale thickness," *Appl. Phys. Lett.*, vol. 84, no. 11, pp. 1976–1978, Mar. 2004.
[5] A. P. Davila, J. Jang, A. K. Gupta, T. Walter, A. Aronson, and R. Bashir, "Microresonator mass sensors for detection of Bacillus anthracis Sterne spores in air and water," *Biosens. Bioelectron.*, vol. 22, no. 12, pp. 3028–3035, Jun. 2007.
[6] K. Y. Gfeller, N. Nugaeva, and M. Hegner, "Micromechanical oscillators as rapid biosensor for the detection of active growth of Escherichia coli," *Biosens. Bioelectron.*, vol. 21, no. 3, pp. 528–533, Sep. 2005.
[7] N. Nugaeva, K. Y. Gfeller, N. Backmann, H. P. Lang, M. Duggelin, and M. Hegner, "Micromechanical cantilever array sensors for selective fungal immobilization and fast growth detection," *Biosens. Bioelectron*, vol. 21, no. 6, pp. 849–856, Dec. 2005.
[8] N. Nugaeva, K. Y. Gfeller, N. Backmann, M. Duggelin, H. P. Lang, H. J. Guntherodt, and M. Hegner, "An antibody-sensitized microfabricated cantilever for the growth detection of Aspergillus niger spores," *Microsc. Microanal.*, vol. 13, no. 1, pp. 13–17, Feb. 2007.
[9] K. Park, L. J. Millet, N. Kim, H. Li, X. Jin, G. Popescua, N. R. Aluru, K. J. Hsia, and R. Bashir, "Measurement of adherent cell mass and growth," *Proc. Nat. Acad. Sci. U.S.A.*, vol. 107, no. 48, pp. 20 691–20 696, Nov. 2010.
[10] T. P. Burg, M. Godin, S. M. Knudsen, W. Shen, G. Carlson, J. S. Foster, K. Babcock, and S. R. Manalis, "Weighing of biomolecules, single cells and single nanoparticles in fluid," *Nature*, vol. 446, no. 7139, pp. 1066–1069, Apr. 2007.
[11] M. Godin, F. F. Delgado, S. Son, W. H. Grover, A. K. Bryan, A. Tzur, P. Jorgensen, K. Payer, A. D. Grossman, M. W. Kirschner, and S. R. Manalis, "Using buoyant mass to measure the growth of single cells," *Nat. Methods*, vol. 7, no. 5, pp. 387–390, May 2010.
[12] A. F. M. Leenaars, J. A. M. Heuthorst, and J. J. V. Oekel, "Marangoni drying: A new extremely clean drying process," *Langmuir*, vol. 6, no. 11, pp. 1701–1703, Nov. 1990.
[13] J. Marra and J. A. M. Heuthorst, "Physical principles of Marangoni drying," *Langmuir*, vol. 7, no. 11, pp. 2748–2755, Nov. 1991.
[14] A. Thess and W. Boos, "A model for Marangoni drying," *Phys. Fluids*, vol. 11, no. 12, pp. 3852–3855, Dec. 1999.

[15] J. Park and J. Moon, "Control of colloidal particle deposit patterns with picoliter droplets ejected by ink-jet printing," *Langmuir*, vol. 22, no. 8, pp. 3506–3513, Apr. 2006.
[16] J. A. Lim, W. H. Lee, H. S. Lee, J. H. Lee, Y. D. Park, and K. Cho, "Self-organization of ink-jet-printed triisopropylsilylethynyl pentacene via evaporation-induced flows in a drying droplet," *Adv. Funct. Mater.*, vol. 18, no. 2, pp. 229–234, Jan. 2008.
[17] J. Jing, J. Reed, J. Huang, X. Hu, V. Clarke, J. Edington, D. Housman, T. S. Anantharamani, E. J. Huff, B. Mishrai, B. Porter, A. Shenker, E. Wolfson, C. Hiort, R. Kantor, C. Aston, and D. C. Schwartz, "Automated high resolution optical mapping using arrayed, fluid-fixed DNA molecules," *Proc. Nat. Acad. Sci. U.S.A.*, vol. 95, no. 14, pp. 8046–8051, Jul. 1998.
[18] M. Chopra, L. Li, H. Hu, M. A. Burns, and R. G. Larson, "DNA molecular configurations in an evaporating droplet near a glass surface," *J. Rheology*, vol. 47, no. 5, pp. 1111–1132, Sep. 2003.
[19] R. D. Deegan, O. Bakajin, T. F. Dupont, G. Huber, S. R. Nagel, and T. A. Witten, "Contact line deposits in an evaporating drop," *Phys. Rev. E*, vol. 62, no. 1, pp. 756–765, Jul. 2000.
[20] H. Hu and R. G. Larson, "Analysis of the microfluid flow in an evaporating sessile droplet," *Langmuir*, vol. 21, no. 9, pp. 3963–3971, Apr. 2005.
[21] F. Girard, M. Antoni, S. Faure, and A. Steinchen, "Evaporation and marangoni driven convection in small heated water droplets," *Langmuir*, vol. 22, no. 26, pp. 11 085–11 091, Dec. 2006.
[22] G. J. Dunn, S. K. Wilson, B. R. Duffy, S. David, and K. Sefiane, "The effect of the thermal conductivity of the substrate on droplet evaporation," *Math. Ind.*, vol. 12, pp. 779–783, 2008.
[23] H. Hu and R. G. Larson, "Evaporation of a sessile droplet on a substrate," *J. Phys. Chem*, vol. 106, no. 6, pp. 1334–1344, Feb. 2002.
[24] S. Dohn, R. Sandberg, W. Svendsen, and A. Boisen, "Enhanced functionality of cantilever based mass sensors using higher modes," *Appl. Phys. Lett.*, vol. 86, no. 23, pp. 233 501–233 501-3, Jun. 2005.
[25] S. Dohn, W. Svendsen, A. Boisen, and O. Hansen, "Mass and position determination of attached particles on cantilever based mass sensors," *Rev. Sci. Instrum.*, vol. 78, no. 10, p. 103303, Oct. 2007.
[26] K. N. Marsh, *Recommended Reference Materials for the Realization of Physicochemical Properties*. Oxford, U.K.: Wiley-Blackwell, 1987.
[27] T. B. Douglas, "Vapor pressure of methyl sulfoxide from 20 to 50°. Calculation of the heat of vaporization," *J. Amer. Chem. Soc.*, vol. 70, no. 6, pp. 2001–2002, Jun. 1948.
[28] E. W. Lemmon, M. O. McLinden, and D. G. Friend, NIST Chemistry WebBook, 2003. [Online]. Available: http://webbook.nist.gov

Kidong Park received the B.S. degree in electrical engineering from Seoul National University, Seoul, Korea, in 1999, and the Ph.D. degree in electrical and computer engineering from Purdue University, West Lafayette, IN, in 2009.

From 2009 to 2010, he was a Postdoctoral Research Associate with the Micro and Nanotechnology Laboratory, University of Illinois at Urbana–Champaign (UIUC), Urbana. From January 2011 to October 2011, he was a Senior Engineer with Samsung Electronics. He is currently a Postdoctoral Research Associate with the Micro and Nanotechnology Laboratory, UIUC, where he is also with the Department of Electrical and Computer Engineering. His current research interests include modeling, design, fabrication, and characterization of biomicroelectromechanical systems sensors and microfluidic devices for medical diagnostic and cellular studies.

Namjung Kim received the B.S. degree in mechanical engineering from the Korea Advanced Institute of Science and Engineering, Daejeon, Korea, in 2007, and the M.S. degree from Carnegie Mellon University, Pittsburgh, PA, in 2009. He is currently working toward the Ph.D. degree in the Department of Mechanical Science and Engineering, University of Illinois at Urbana–Champaign, Urbana.

Dallas T. Morisette received the B.S. degree in electrical engineering from Walla Walla College, College Place, WA, in 1993, and the M.S.E.E. degree and the Ph.D. degree (for his work on the development of silicon carbide Schottky diodes) from Purdue University, West Lafayette, IN, in 1997 and 2001, respectively.

Since then, he has pursued research interests in microelectronics, optoelectronics, and biomicroelectromechanical systems devices both as a Research Scientist at Purdue University and at two West Lafayette-based start-up companies. He is currently a Senior Research Scientist with Group 4 Development, LLC, West Lafayette, seeking to develop graphene-based electronic devices and materials.

N. R. Aluru received the B.E. degree (with honors and distinction) from Birla Institute of Technology and Science, Pilani, India, in 1989, the M.S. degree from Rensselaer Polytechnic Institute, Troy, NY, in 1991, and the Ph.D. degree from Stanford University, Stanford, CA, in 1995.

From 1995 to 1997, he was a Postdoctoral Associate at Massachusetts Institute of Technology, Cambridge. In 1998, he joined the University of Illinois at Urbana–Champaign (UIUC), Urbana, as an Assistant Professor. He is currently the Richard W. Kritzer Professor in the Department of Mechanical Science and Engineering, UIUC. He is also with the Beckman Institute for Advanced Science and Technology, the Department of Electrical and Computer Engineering, and the Bioengineering Department, UIUC. He currently serves on the Editorial Board of *Computer Methods in Applied Mechanics and Engineering* and a number of other journals.

Dr. Aluru was a recipient of a National Science Foundation CAREER Award in 1999, the NCSA Faculty Fellowship in 1999 and 2006, the 2001 CMES Distinguished Young Author Award, the Xerox Award for Faculty Research in 2002, the American Society of Mechanical Engineers (ASME) Gustus L. Larson Memorial Award in 2006, and the United States Association for Computational Mechanics (USACM) Gallagher Young Investigator Award in 2007. He was recognized as a Willett Faculty Scholar by the College of Engineering, UIUC, for the period of 2002–2008 and a University Scholar in 2010. He is a Subject Editor of the JOURNAL OF MICROELECTROMECHANICAL SYSTEMS and served as an Associate Editor of the IEEE TRANSACTIONS ON CIRCUITS AND SYSTEMS II for 2004–2005. He is a Fellow of USACM and ASME.

Rashid Bashir (S'90–M'92–SM'00–F'09) received the B.S.E.E. degree from Texas Tech University, Lubbock, in 1987, and the M.S.E.E. and Ph.D. degrees from Purdue University, West Lafayette, IN, in 1989 and 1992, respectively.

From October 1992 to October 1998, he was a Senior Engineering Manager with the Analog/Mixed Signal Process Technology Development Group, National Semiconductor. In October 1998, he joined Purdue University as an Assistant Professor and was later promoted to a Professor of electrical and computer engineering and a Courtesy Professor of biomedical engineering and mechanical engineering. He was the recipient of the NSF Faculty Early Career Award in 2000, the Ruth and Joel Spira Outstanding Teaching Award from Purdue University in 2000, and was a Purdue University Faculty Scholar from 2005–2007. Since October 2007, he has been the Abel Bliss Professor in the Department of Electrical and Computer Engineering and the Department of Bioengineering, University of Illinois at Urbana–Champaign, Urbana, where he is also the Director of the Micro and NanoTechnology Laboratory (a campus-wide clean room facility). He has authored or coauthored over 130 journal papers, over 160 conference papers and conference abstracts, and over 90 invited talks and is the holder of 34 patents. His research interests include bionanotechnology, biomicroelectromechanical systems, laboratory on a chip, interfacing biology and engineering from molecular to tissue scale, and applications of semiconductor fabrication to biomedical engineering, all applied to solve biomedical problems. He currently serves as an Associate Editor of the IEEE TRANSACTIONS ON BIOMEDICAL ENGINEERING and *Biomedical Microdevices*.

Dr. Bashir is a Fellow of AIMBE and AAAS.